

Structure, luminescence of Eu^{2+} and Eu^{3+} in $\text{CaMgSi}_2\text{O}_6$ and their co-existence for the excitation-wavelength/temperature driven colour evolution

Su, Fang; Zhou, Weijie; Yang, Yunlin; Ou, Yiyi; Qi, Zeming; Duan, Chang Kui; Brik, Mikhail G.; Dorenbos, Pieter; Liang, Hongbin

DOI

[10.1039/d1dt01377g](https://doi.org/10.1039/d1dt01377g)

Publication date

2021

Document Version

Final published version

Published in

Dalton Transactions

Citation (APA)

Su, F., Zhou, W., Yang, Y., Ou, Y., Qi, Z., Duan, C. K., Brik, M. G., Dorenbos, P., & Liang, H. (2021). Structure, luminescence of Eu^{2+} and Eu^{3+} in $\text{CaMgSi}_2\text{O}_6$ and their co-existence for the excitation-wavelength/temperature driven colour evolution. *Dalton Transactions*, 50(29), 10050-10058. <https://doi.org/10.1039/d1dt01377g>

Important note

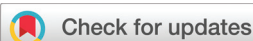
To cite this publication, please use the final published version (if applicable). Please check the document version above.

Copyright

Other than for strictly personal use, it is not permitted to download, forward or distribute the text or part of it, without the consent of the author(s) and/or copyright holder(s), unless the work is under an open content license such as Creative Commons.

Takedown policy

Please contact us and provide details if you believe this document breaches copyrights. We will remove access to the work immediately and investigate your claim.

Cite this: *Dalton Trans.*, 2021, **50**, 10050

Structure, luminescence of Eu^{2+} and Eu^{3+} in $\text{CaMgSi}_2\text{O}_6$ and their co-existence for the excitation-wavelength/temperature driven colour evolution†

Fang Su,^a Weijie Zhou,^b Yunlin Yang,^a Yiyi Ou,^a Zeming Qi,^b Chang-Kui Duan,^b Mikhail G. Brik,^{c,d,e} Pieter Dorenbos^f and Hongbin Liang^{*,a}

Luminescent materials with controllable colour evolution features are demanded for the development of multi-level anti-counterfeiting technologies. Here we report the structural and luminescence properties of $\text{CaMgSi}_2\text{O}_6:\text{Ln}$ ($\text{Ln} = \text{Eu}^{2+}$, Eu^{3+} , $\text{Eu}^{2+/3+}$) samples in detail and reveal their excitation-wavelength/temperature driven colour evolution characteristics. By tuning either the excitation-wavelength (276, 304, 343, 394 nm) or temperature (in the 330–505 K range), the designed samples with co-existing $\text{Eu}^{2+}/\text{Eu}^{3+}$ ions can achieve diverse and controllable colour evolution from red, to pink, purple and blue. This shows their potential application in anti-counterfeiting with the help of sophisticated pattern design. In addition, the underlying mechanism of the Stokes shift of the Eu^{2+} emission and valence stability of both $\text{Eu}^{2+}/\text{Eu}^{3+}$ ions in $\text{CaMgSi}_2\text{O}_6$ are also studied in depth. These results are valuable for designing colour-controllable luminescent materials based on the co-existence of the $\text{Eu}^{2+}/\text{Eu}^{3+}$ ions for anti-counterfeiting applications.

Received 26th April 2021,
Accepted 8th June 2021

DOI: 10.1039/d1dt01377g

rsc.li/dalton

1. Introduction

Anti-counterfeiting technologies have attracted more and more attention in recent years.^{1,2} Among the different methods and techniques used in anti-counterfeiting, luminescence is one of the most widely used. Lanthanide ions are essential luminescent centers in these materials.^{3,4} As one of the lanthanide ions, europium can exist as divalent Eu^{2+} or trivalent Eu^{3+} in luminescent materials, and their luminescence characteristics are quite different. Eu^{3+} is a typical lanthanide ion with the 4f–

4f transitions having sharp line-like red emissions.⁵ In contrast, the Eu^{2+} ions display the 5d–4f emission when its lowest 4f⁶5d state is below the ⁶P_J levels ($J = 3/2, 5/2, 7/2$) in energy.^{6,7} The colour of the broad 5d–4f emission of the Eu^{2+} ions varies over a wide range, usually from violet to red in common host compounds, depending on various parameters, such as the nephelauxetic effect, crystal field strength, effective phonon energy and the Huang–Rhys parameter.^{8–11} In a properly chosen host compound, both Eu^{2+} and Eu^{3+} ions can coexist and produce emissions of matching or comparable intensities with different colours. In such a case, the whole (combined) emission colour of the $\text{Eu}^{2+}/\text{Eu}^{3+}$ co-doped material can be tuned by changing the excitation wavelengths. The approach would be a simple way for anti-counterfeiting, and this anti-counterfeiting characteristic can be further enhanced by the different thermal quenching properties of the Eu^{2+} and Eu^{3+} luminescence.

The alkaline earth silicates have been known for quite some time as good host compounds for a number of luminescent materials due to their excellent physical, chemical, thermal stability and optical properties.^{12,13} In particular, the calcium magnesium silicate, $\text{CaMgSi}_2\text{O}_6$, of monoclinic structure has attracted great attention because of its special structural features, excellent solubility of lanthanide ions and good bio-compatibility.^{14–18}

^aMOE Key Laboratory of Bioinorganic and Synthetic Chemistry, KLGHEI of Environment and Energy Chemistry, School of Chemistry, Sun Yat-sen University, Guangzhou 510275, P. R. China. E-mail: cesbin@mail.sysu.edu.cn; Tel: +86 20 84113695

^bNational Synchrotron Radiation Laboratory, Hefei National Laboratory for Physical Sciences at the Microscale and School of Physical Sciences, University of Science and Technology of China, Hefei 230029, P. R. China

^cCollege of Sciences & CQUPT-BUL Innovation Institute, Chongqing University of Posts and Telecommunications, Chongqing 400065, P. R. China

^dInstitute of Physics, University of Tartu, Tartu 50411, Estonia

^eInstitute of Physics, Jan Długość University, PL-42200 Częstochowa, Poland

^fFaculty of Applied Sciences, Delft University of Technology, 2629 JB, Delft, The Netherlands

† Electronic supplementary information (ESI) available. See DOI: 10.1039/d1dt01377g

To provide a sound support for the possible applications of the Eu^{2+} and Eu^{3+} doped $\text{CaMgSi}_2\text{O}_6$ materials in anti-counterfeiting, in this work we investigate the vacuum ultraviolet-ultraviolet-visible (VUV-UV-vis) luminescence and thermal quenching characteristics of both Eu^{2+} and Eu^{3+} impurities, discuss the electron-vibrational interaction (EVI) for the Eu^{2+} 5d states, construct the vacuum referred binding energy (VRBE) scheme of all trivalent/divalent lanthanide ions in this material and elucidate the europium redox properties in the host compound. The results reveal that different colour emissions can be realized with a single europium doping in a single-phase $\text{CaMgSi}_2\text{O}_6$ material under different wavelengths excitation, and the emission colour evolution can be further enhanced by varied temperatures, demonstrating the possible application of this material in excitation-wavelength and temperature driven dual models of anti-counterfeiting.

2. Experimental section

Powder samples with nominal chemical formulae $\text{CaMgSi}_2\text{O}_6$, $\text{Ca}_{0.998}\text{Ln}_{0.001}\text{Na}_{0.001}\text{MgSi}_2\text{O}_6$ ($\text{Ln} = \text{Ce}^{3+}$, Eu^{3+} , Tb^{3+}) and $\text{Ca}_{1-x}\text{Eu}_x\text{MgSi}_2\text{O}_6$ ($x = 0.001$, 0.02) were prepared *via* a high-temperature solid-state reaction method. The raw materials including CaCO_3 (A.R.), $4\text{MgCO}_3 \cdot \text{Mg}(\text{OH})_2 \cdot 5\text{H}_2\text{O}$ (A.R.), SiO_2 (99.99%), CeO_2 (99.99%), Eu_2O_3 (99.99%) and Tb_4O_7 (99.99%) were weighed stoichiometrically and ground thoroughly in an agate mortar using alcohol as the mixing medium. Suitable amounts of NH_4Cl (A.R.) and Na_2CO_3 (A.R.) were also added as flux and charge compensator for the aliovalent doping of $\text{Ce}^{3+}/\text{Eu}^{3+}/\text{Tb}^{3+}$ ions on Ca^{2+} sites, respectively. The homogeneous mixtures were then sintered under CO reducing, N_2 inert or air oxidizing ambiances at 1150°C for 6 h, respectively. The final products were obtained after cooling down to room temperature (RT).

The powder X-ray diffraction (XRD) patterns of the synthesized samples were recorded on a Rigaku D-MAX 2200 VPC X-ray diffractometer with $\text{Cu K}\alpha$ radiation ($\lambda = 1.5418 \text{ \AA}$) at 40 kV and 26 mA. The scanning speed was $10^\circ \text{ min}^{-1}$. As for the high quality XRD data for the Rietveld refinement, they were collected on a Bruker D8 Advance powder diffractometer using a step size of $0.4^\circ \text{ min}^{-1}$ in a 2θ range of 5° – 110° with the $\text{Cu K}\alpha$ X-ray tube operated at 40 kV and 40 mA. The refinement was performed using the TOPAS-Academic software.¹⁹ The excitation/emission spectra of the doped samples in the VUV-UV range were recorded at the beamline 4B8 of the Beijing Synchrotron Radiation Facility (BSRF), and those in the UV-vis range as well as luminescence decay curves were recorded by the Edinburgh FLS 1000 combined fluorescence lifetime and steady state spectrometer. A 450 W Xe 900 lamp was used as the excitation source for the steady-state spectra, and a 150 W F920 ns flash-lamp with a pulse width of less than 3 ns and a pulse repetition rate of 40 kHz was used to collect the luminescence decay curves. The sample temperature was monitored by a temperature controller (Oxford, CRYTEMP).

The morphology, composition and elemental mapping of the prepared host sample were analysed using a field-emission scanning electron microscope (FE-SEM, Gemini 500) equipped with elemental distribution mapping techniques.

The Raman spectrum was collected using a laser micro-Raman spectrometer with a resolution of 1 cm^{-1} , and the far-infrared (IR) reflection spectrum was measured on the U4 beamline of the National Synchrotron Radiation Laboratory (NSRL, Hefei, China).

3. Results and discussion

3.1. Morphology and crystal structure

Fig. 1a shows the Rietveld refinement result of the high-quality XRD pattern of the synthesized $\text{CaMgSi}_2\text{O}_6$ compound using the monoclinic structure with the $C2/c$ space group (ICSD-159048) as the initial fitting model.²⁰ No apparent impurity peaks were found and the obtained reliability factors are $R_{\text{wp}} = 2.58\%$, $R_p = 1.56\%$ and $R_B = 2.90\%$, which indicate the successful synthesis of the $\text{CaMgSi}_2\text{O}_6$ purity phase. The refined lattice parameters are $a = 9.747 (1) \text{ \AA}$, $b = 8.932 (1) \text{ \AA}$, $c = 5.249 (1) \text{ \AA}$, $\beta = 105.9^\circ$, $V = 439.6 \text{ \AA}^3$ and $Z = 4$. The refined structural parameters of the $\text{CaMgSi}_2\text{O}_6$ compound are listed in Table 1. Fig. 1b presents the crystal structure and coordination environment of the Ca^{2+} site. There is only one Ca^{2+} crystallographic site surrounded by eight neighbouring O^{2-} ions with the C_2 symmetry to form a $[\text{CaO}_8]$ dodecahedron with the average Ca^{2+} – O^{2-} bond distance of 2.501 \AA , and the nearest distance between two adjacent Ca^{2+} ions is 4.412 \AA . The Mg^{2+} ions are coordinated by six O^{2-} ions and the Si^{4+} ions are coordinated by four O^{2-} ions. The $[\text{CaO}_8]$, $[\text{MgO}_6]$ and $[\text{SiO}_4]$ polyhedra share their corners to construct the $\text{CaMgSi}_2\text{O}_6$ structural framework. In addition, the morphology and composition of the synthesized $\text{CaMgSi}_2\text{O}_6$ compound are investigated by SEM as shown in Fig. 1c. The sample particles have an irregular shape with a size of 2–3 μm , and the elemental-mapping results further show the uniform distributions of the elements Ca, Mg, Si and O. Finally, the typical XRD patterns of the doped samples are depicted in Fig. 1d. All the patterns are similar and show good consistency with the standard PDF card #78-1390 of $\text{CaMgSi}_2\text{O}_6$, which implies that these doped samples are single phase pure and the doping of Na^+ and $\text{Eu}^{2+/3+}$ ions does not significantly affect the structure of the $\text{CaMgSi}_2\text{O}_6$ host compound. Considering the similar ionic radii of Ca^{2+} ($\sim 1.12 \text{ \AA}$), Na^+ ($\sim 1.18 \text{ \AA}$), Ce^{3+} (1.14 \AA), Eu^{3+} (1.07 \AA) and Eu^{2+} ($\sim 1.25 \text{ \AA}$) in the eight-fold coordination,²¹ it is expected that the doping ions enter the Ca^{2+} sites.

3.2. Luminescence and electron-vibrational interaction of the Eu^{2+} ions

Fig. 2 shows the normalized low-temperature VUV-UV excitation ($\lambda_{\text{em}} = 451 \text{ nm}$) spectra of the $\text{Ca}_{0.999}\text{Eu}_{0.001}\text{MgSi}_2\text{O}_6$ sample prepared in a CO reducing ambience using a synchrotron radiation VUV light source (curve a) and a xenon lamp (curve b), respectively. The H band with a maximum at ~ 7.90

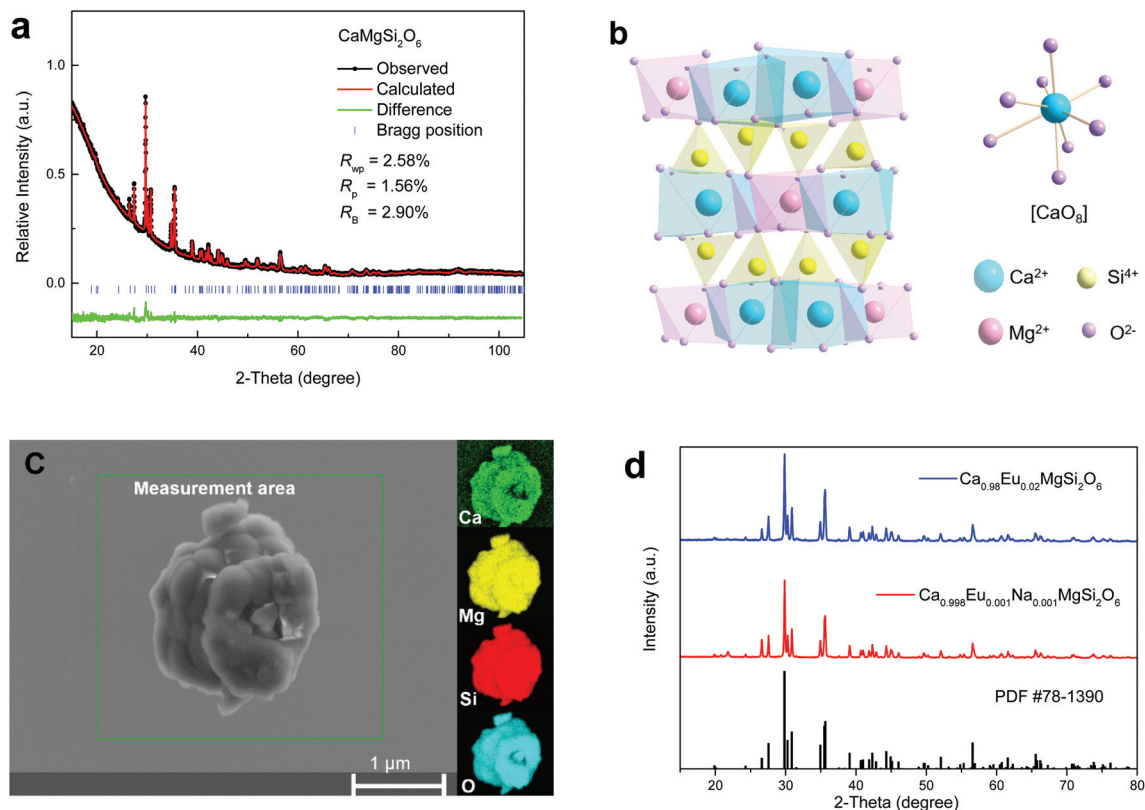


Fig. 1 (a) Rietveld refinement of high-quality XRD data of $\text{CaMgSi}_2\text{O}_6$ compound at RT. (b) Crystal structure of $\text{CaMgSi}_2\text{O}_6$ compound with the coordination environment of Ca^{2+} site. (c) SEM image of $\text{CaMgSi}_2\text{O}_6$ compound and the corresponding elemental mapping. (d) Typical XRD patterns of doped samples at RT.

Table 1 Refined structural parameters of $\text{CaMgSi}_2\text{O}_6$ ^a compound

Atom	Wyck.	x	y	z	Occ.
Ca	4e	0	0.9080	0.2500	1
Mg	4e	0	0.3015	0.2500	1
Si	8f	0.2861	0.09318	0.2293	1
O (1)	8f	0.1155	0.08690	0.1418	1
O (2)	8f	0.3609	0.2501	0.3177	1
O (3)	8f	0.3507	0.01744	0.9954	1

^a Symmetry: monoclinic; space group: $C2/c$; lattice parameters: $a = 9.747$ (1) Å, $b = 8.932$ (1) Å, $c = 5.249$ (1) Å, $\alpha = \gamma = 90^\circ$, $\beta = 105.866^\circ$, $V = 439.6$ Å³, $Z = 4$.

eV (~ 157 nm) is due to the host excitonic absorption of the $\text{CaMgSi}_2\text{O}_6$ compound, which is in line with that observed in the Ce^{3+} doped sample.²² The bands below ~ 5.90 eV (210 nm) are the results of the $4f^7-4f^65d^1$ transitions of Eu^{2+} ions as mentioned in ref. 22. The f-d excitation spectrum of Eu^{2+} is much more complex than that of Ce^{3+} due to the influences of several factors. Firstly, the 5d electron in the $4f^65d$ excited state of Eu^{2+} experiences crystal field splitting (CFS). The CFS patterns of Ce^{3+} and Eu^{2+} are similar, but the CFS magnitude of Eu^{2+} is usually about two thirds of that of Ce^{3+} .²³ Secondly, the lowest states of the $4f^6$ core electron configuration in each $4f^65d$ excited state of Eu^{2+} can be further split into seven

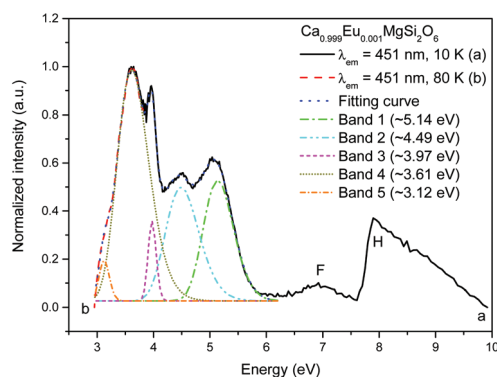


Fig. 2 The VUV-UV excitation (a, $\lambda_{\text{em}} = 451$ nm, 10 K; b, $\lambda_{\text{em}} = 451$ nm, 80 K) spectra of sample $\text{Ca}_{0.999}\text{Eu}_{0.001}\text{MgSi}_2\text{O}_6$ prepared in CO reducing ambience and the fitting results by using the sum of five Gaussian functions.

7F_J ($J = 0-6$) multiplets by spin-orbit coupling, which broadens each $4f^65d$ excited band into an about 5000 cm^{-1} (~ 0.62 eV) wide non-Gaussian “staircase” structure. In addition, there is the interaction between the 5d electron and the remaining $4f^6$ core electrons of Eu^{2+} and so on.²⁴⁻²⁶ As a consequence, the $4f^7-4f^65d^1$ excitation spectrum of Eu^{2+} in $\text{CaMgSi}_2\text{O}_6$ should contain numerous overlapping bands. To roughly estimate the

crystal field splitting (CFS) of the Eu^{2+} 5d state, the merged excitation profile in ~ 2.95 – 5.90 eV (~ 210 – 420 nm) range is fitted to a sum of five Gaussian functions because Eu^{2+} ions are assumed to occupy $[\text{CaO}_8]$ sites with low C_2 symmetry. The peaks of those five bands are at about 5.14, 4.49, 3.97, 3.61 and 3.12 eV, respectively. Although the intensity (area) of the band at 3.12 or 3.97 eV shows a large difference from that at 3.61 eV and the band at 3.97 eV is too narrow in the fitting result, the estimated CFS ~ 2.02 eV of Eu^{2+} is ~ 0.774 times that of Ce^{3+} in $\text{CaMgSi}_2\text{O}_6$ (~ 2.61 eV).²² This ratio is a typical value of the CFS of Eu^{2+} ions relative to that of Ce^{3+} , and it seems that the fitting result provides an acceptable estimation of the CFS value. Besides, the observation implies that the emissions of Ce^{3+} and Eu^{2+} result from the same kind of single lattice site.²³ Meanwhile, the lowest $4f^65d^1$ energy can be evaluated by different methods except for the above estimated 3.12 eV. Due to the large Stokes shift of Eu^{2+} luminescence in the present case (see Fig. 2 and 3a and discussions), it is impossible to estimate this value by using the intersection point of the excitation and emission spectra. We first consider the spin-orbit coupling of 7F_J in the $4f^6[{}^7F_J]5d^1$ excited state of Eu^{2+} . In this way, the lowest $4f^65d^1$ energy is evaluated as ~ 2.99 eV if we approximately consider the main peak (~ 3.61 eV) as the transition from the lowest 5d state to the 7F_6 multiplet by subtracting the 7F_J ($J = 0, 6$) energy difference of ~ 5000 cm^{-1} (0.62 eV) from the main peak.²⁶ This value is in good agreement with the empirical estimation (~ 3.03 eV), when we regard the 15–20% of the maximum height on the low energy side as the first $4f^65d^1$ transition.²³ Based on these data, we take the median value 3.03 eV of three estimations 2.99, 3.03 and 3.12 eV as the lowest $4f^65d^1$ energy in the following discussions. As for the F band at about 177 nm in Fig. 2, it may be attributed to the excited state of some defect in the sample rather than to the undetected impurity phase. This assumption is supported by the similar emission profile of Eu^{2+} ions when excited by 177 nm and other 5d excitation wavelengths from 310 to 360 nm (Fig. S1†).

Fig. 3a shows the emission ($\lambda_{\text{ex}} = 356$ nm) spectrum of the sample $\text{Ca}_{0.999}\text{Eu}_{0.001}\text{MgSi}_2\text{O}_6$ at 80 K. The narrow emission

band at ~ 2.75 eV (~ 451 nm) is with a full width at half maximum (FWHM) about 0.20 eV. Accordingly, the Stokes shift for the Eu^{2+} ions in $\text{CaMgSi}_2\text{O}_6$ is calculated to be ~ 0.28 eV using the energy difference between the maxima of the estimated lowest 5d excitation band (~ 3.03 eV) and the emission band (~ 2.75 eV). This value is the same as that of Ce^{3+} (~ 0.28 eV).²² Empirically, the Stokes shift of Eu^{2+} is 0.61 ± 0.03 times that of Ce^{3+} in the same host site, the mismatch in the present case may result from the error in the evaluation of the lowest $4f^65d^1$ energy.²³

In fact, the Stokes shift for the Eu^{2+} 4f–5d transition is usually related to the electron-vibrational interaction (EVI) and composed by the contributions of energy relaxation in the Eu^{2+} excited and ground states in the configurational coordination model. A weak EVI always results in the small Stokes shift along with the narrow bandwidth of Eu^{2+} emission.²⁷

The relationship of the Stokes shift and the bandwidth at half maximum (FWHM, Γ) of Eu^{2+} emission can be described in the framework of the Huang–Rhys theory as given below:^{28,29}

$$E_s = (2S - 1)\hbar\omega \quad (1)$$

$$\Gamma(T) = \sqrt{8\ln 2\hbar\omega} \left[S \cdot \coth\left(\frac{\hbar\omega}{2kT}\right) \right]^{1/2} \quad (2)$$

where T is the temperature in Kelvin, k is the Boltzmann constant [8.62×10^{-5} (eV K) $^{-1}$], S is the Huang–Rhys factor, and $\hbar\omega$ is the effective phonon energy which interacts with the 4f–5d electronic transition of Eu^{2+} . We first collect the emission spectra of the $\text{Ca}_{0.999}\text{Eu}_{0.001}\text{MgSi}_2\text{O}_6$ sample in the temperature range of 80–430 K in Fig. S2,† showing that the emission band becomes broader and the intensity decreases with increasing temperature, and the activation energy (E_a) of the thermal-quenching of Eu^{2+} luminescence has been estimated as ~ 0.298 eV.²² Then we extract the temperature-dependent FWHM values of Eu^{2+} emission from Fig. S2† and show them in Fig. 3b. They can be well fitted using eqn (2) above and the factors S and $\hbar\omega$ are also obtained as ~ 3.39 and $\sim 4.62 \times 10^{-2}$ eV (~ 373 cm^{-1}), respectively. Based on these two factors, the

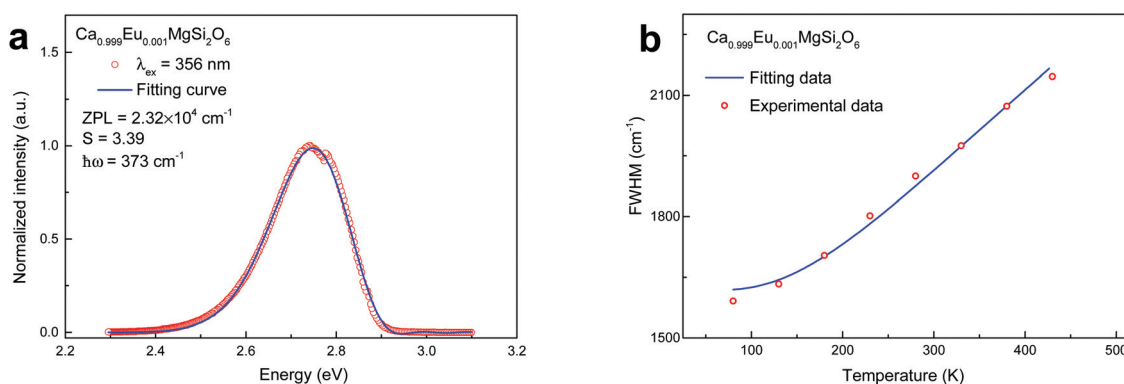


Fig. 3 (a) The emission ($\lambda_{\text{ex}} = 356$ nm) spectrum of Eu^{2+} in the sample $\text{Ca}_{0.999}\text{Eu}_{0.001}\text{MgSi}_2\text{O}_6$ at 80 K and fitting curve. (b) Temperature-dependent FWHM values of Eu^{2+} emission in the temperature range of 80–430 K and fitting curve.

emission profile of Eu^{2+} at 80 K can be simulated using eqn (3) which describes the vibronic bands with a “Pekar” type spectral distribution as presented in Fig. 3a:²⁸

$$I = \frac{e^{-S} S^p}{p!} \left(1 + S^2 \frac{e^{-\frac{\hbar\omega}{kT}}}{p+1} \right), p = \frac{E_0 - E}{\hbar\omega} \quad (3)$$

where E_0 is the zero-phonon line energy for the emission process and p is the number of effective phonons involved in the coupling process between the Eu^{2+} ions and the host compound. When E_0 is set as ~ 2.88 eV, the best simulation of Eu^{2+} emission spectrum can be achieved, this value is consistent with the onset energy of the experimental Eu^{2+} emission spectrum. In addition, the obtained $\hbar\omega$ value is also located in the possible vibrational energy range (below 500 cm^{-1}) of the cationic coordination environment (Ca/Eu–O) as shown in Fig. S3.† All results imply that the obtained S and $\hbar\omega$ values are reliable and could adequately reflect the EVI between the Eu^{2+} 5d states and the $\text{CaMgSi}_2\text{O}_6$ host. Finally, by applying eqn (1), we derive that the Stokes shift is equal to ~ 0.27 eV, which is in good agreement with that mentioned above (~ 0.28 eV).

3.3. Luminescence of the Eu^{3+} ions

The excitation ($\lambda_{\text{em}} = 614$ nm) spectra of the $\text{Ca}_{0.998}\text{Eu}_{0.001}\text{Na}_{0.001}\text{MgSi}_2\text{O}_6$ sample prepared in an air atmosphere were collected using a synchrotron radiation VUV light source and xenon lamp at RT, respectively, as shown in Fig. 4. In this sample, Na^+ ions provided by Na_2CO_3 act as charge compensators to keep the formal charge balance of the sample, due to the aliovalent substitution of trivalent Eu^{3+} for divalent Ca^{2+} ions. Due to the similarity of the ionic radii, the charge compensators may occupy the lattice sites of Ca^{2+} ions, but actually we cannot exclude the presence of interstitials, vacancies and/or other defects in the sample.

The absorption band at ~ 164 nm is aligned to the host absorption band (~ 157 nm) as discussed in Fig. 2, the slight shift (~ 7 nm) may be due to the influence of the CTB. The band located at ~ 239 nm (5.19 eV) can be attributed to the O^{2-}

$\rightarrow \text{Eu}^{3+}$ charge transfer band (CTB). The sharp peaks above 300 nm correspond to the intra-configurational 4f–4f transition of Eu^{3+} ions, and the strongest one at ~ 394 nm is ascribed to the ${}^7\text{F}_0\text{--}{}^5\text{L}_6$ transition. Under 394 nm excitation, the emission spectrum of Eu^{3+} ions in Fig. 4 contains the characteristic five sets of the 4f–4f sharp emission peaks corresponding to the ${}^5\text{D}_0 \rightarrow {}^7\text{F}_J$ ($J = 0, 1, 2, 3, 4$) transitions respectively, which gives the red colour of characteristic Eu^{3+} emissions.

Further the thermal stability of the Eu^{3+} emissions was studied. The emission ($\lambda_{\text{ex}} = 394$ nm) spectra and luminescence decay ($\lambda_{\text{ex}} = 394$ nm, $\lambda_{\text{em}} = 614$ nm) curves of the $\text{Ca}_{0.998}\text{Eu}_{0.001}\text{Na}_{0.001}\text{MgSi}_2\text{O}_6$ sample in the temperature range of 80–505 K were recorded (Fig. S4†), and the temperature-dependent emission intensities and lifetime values of Eu^{3+} emissions are shown in Fig. S5.† With the increase of temperature, the emission intensity at 505 K remains $\sim 53\%$ of that at ~ 80 K. And the lifetime values of Eu^{3+} emissions seem quite stable when temperature rises. These phenomena indicate that the Eu^{3+} emissions do not experience a strong thermal quenching with rising temperature and thus possess good thermal stability.

The quenching temperature of Eu^{3+} emission is usually related to the charge transfer band (CTB) energy. The higher the CTB energy, the higher the quenching temperature. There appears a more or less linear relationship between quenching temperature and the CTB energy.³⁰ With a CT-energy of 5.19 eV, a quenching temperature T_{50} (the temperature at which the emission intensity drops to 50% of the low temperature value) is expected to be near 900–1000 K, which is consistent with the results in Fig. S5† within the margin of error.

3.4. The co-existence of the Eu^{2+} and Eu^{3+} ions

As discussed in the previous sections, Eu^{2+} luminescence is the main emission in the samples prepared in the CO reducing ambience, while Eu^{3+} emission is dominant in the samples prepared in the air oxidizing atmosphere. Therefore, it is necessary to further discuss the valence states, redox properties and luminescence of europium in the samples prepared in the N_2 inert ambience.

Fig. 5a presents the emission spectra ($\lambda_{\text{ex}} = 276, 343, 394$ nm; RT) of the $\text{Ca}_{0.98}\text{Eu}_{0.02}\text{MgSi}_2\text{O}_6$ sample prepared in the N_2 inert ambience without Na^+ charge compensators. Fig. S6† shows the limited influence of the charge compensators on the emission intensity of $\text{Eu}^{2+/3+}$ in the $\text{Ca}_{1-x}\text{Eu}_x\text{MgSi}_2\text{O}_6$ and $\text{Ca}_{1-2x}\text{Eu}_x\text{Na}_x\text{MgSi}_2\text{O}_6$ ($x = 0.01, 0.02$) samples. Three phenomena are worth mentioning. Firstly, the positions of the peak of the Eu^{2+} emission band and the dominant Eu^{3+} emission line are almost unaffected by the charge compensators. A similar observation is also found in our previous work for $\text{Ba}_2\text{Ca}(\text{BO}_3)_2 \cdot \text{Ce}^{3+}$.³¹ In addition, at a fixed Eu concentration the intensity of the Eu^{2+} emission of the sample without Na^+ is slightly stronger than that with Na^+ , while that of the Eu^{3+} emission shows an opposite tendency, displaying that the incorporation of Na^+ is prone to the stabilization of Eu^{3+} to some extent. In the $\text{CaMgSi}_2\text{O}_6$ crystal, CaO_8 shared its

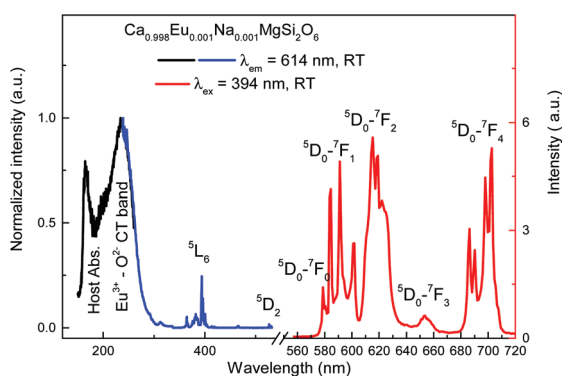


Fig. 4 Excitation ($\lambda_{\text{em}} = 614$ nm) and emission ($\lambda_{\text{ex}} = 394$ nm) spectra of $\text{Ca}_{0.998}\text{Eu}_{0.001}\text{Na}_{0.001}\text{MgSi}_2\text{O}_6$ sample at RT by using synchrotron radiation VUV light source and xenon lamp.

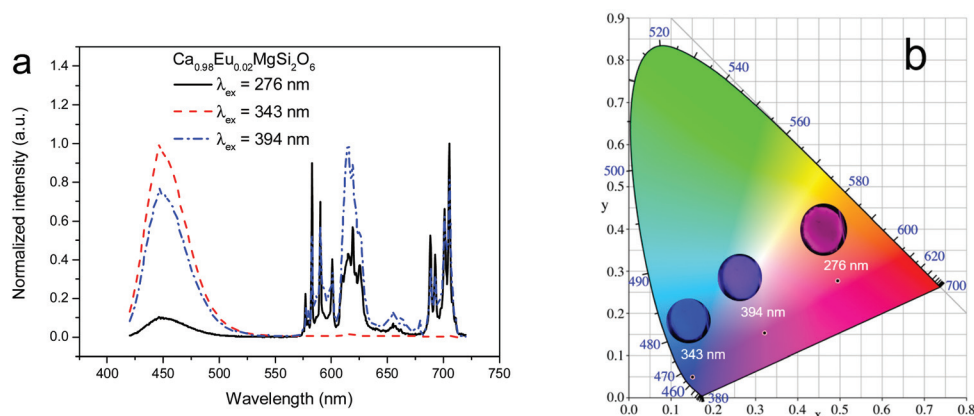


Fig. 5 The emission spectra ($\lambda_{\text{ex}} = 276, 343, 394$ nm) of $\text{Ca}_{0.98}\text{Eu}_{0.02}\text{MgSi}_2\text{O}_6$ sample prepared in N_2 inert ambience (a) and the corresponding CIE colour coordinates and luminescent images (b).

corner O atom with SiO_4 to form the 3D network structure. When trivalent Eu^{3+} ions are incorporated into divalent Ca^{2+} sites, to maintain the electrical neutrality of the compounds, two Eu^{3+} ions should substitute for three Ca^{2+} ions. In this way, one negative Ca^{2+} vacancy V'_{Ca} and two positive defects Eu'_{Ca} would be created. When the samples were prepared at high temperature, the electrons on the Ca^{2+} vacancy V'_{Ca} are activated and captured by the positive defect Eu'_{Ca} , and then Eu^{3+} is reduced to Eu^{2+} . However, the introduction of Na^+ ions could alleviate this process, which causes the decrease of the Eu^{2+} amounts. Finally, due to the influence of the lattice site symmetry, the detailed ${}^5\text{D}_0\text{--}{}^7\text{F}_J$ ($J = 0, 1, 2, 3, 4$) transitions have some variations.

The broad emission band of Eu^{2+} and a group of the sharp line emission of Eu^{3+} are observed in Fig. 5a simultaneously, indicating the presence of both Eu^{2+} and Eu^{3+} ions in the samples prepared in the N_2 ambience. Herein, we first mention the two puzzling points in the emission spectrum under 276 nm excitation (the black solid curve). Firstly, when we consider that the Eu^{3+} ions occupy a C_2 symmetry [CaO_8] site in $\text{CaMgSi}_2\text{O}_6$, the emission intensity of the ${}^5\text{D}_0\text{--}{}^7\text{F}_2$ transition should be stronger than that of the ${}^5\text{D}_0\text{--}{}^7\text{F}_1$ transition since this site is without inversion symmetry. However, we find that the ${}^5\text{D}_0\text{--}{}^7\text{F}_1$ transition is stronger. Secondly, more than one ${}^5\text{D}_0\text{--}{}^7\text{F}_0$ transition lines are observed when we carefully examine the spectrum, which suggests the possible presence of impurities or multi-sites in the samples. But only one Ca^{2+} site is present in the host compound, and the careful checking of the XRD results does not show any impurity also. Further detailed studies on these issues are underway. Here we only discuss the emission intensity variations of Eu^{2+} and Eu^{3+} ions under different wavelength excitations and their potential applications.

The co-existence of the Eu^{2+} and Eu^{3+} ions has attracted extensive attention, and some $\text{Eu}^{2+/3+}$ co-doped phosphors have been reported recently.^{32–35} Usually, these luminescent materials mainly show Eu^{2+} emission under the direct excitation of the Eu^{2+} f-d transition, while the direct excitation of

Eu^{3+} chiefly exhibits Eu^{3+} emission. Further, the possible co-excitation and energy transfer could result in the whole (combined) emission spectra of the $\text{Eu}^{2+/3+}$ co-existence samples. Accordingly, the selection of the excitation wavelength has a significant effect on the emission intensity ratio of Eu^{2+} and Eu^{3+} in the co-doped materials.³³

Referring to Fig. 2 and 4, the $\text{Eu}^{2+} 4f^7 \rightarrow 4f^65d^1$ excitation bands extend from about 210 to 420 nm. The $\text{Eu}^{3+}\text{--O}^{2-}$ charge transfer band (CTB) ranges from about 185 to 300 nm peaking at about 239 nm, and the Eu^{3+} dominant f-f excitation transition is ${}^7\text{F}_0 \rightarrow {}^5\text{L}_6$ at 394 nm. Therefore, three typical excitation wavelengths 276, 343 and 394 nm are selected to measure the emission spectra in Fig. 5a at RT. Since the wavelength 343 nm corresponds to a 4f–5d transition of Eu^{2+} but Eu^{3+} has no significant absorption around this wavelength, the Eu^{2+} emission is considerably strong while that of Eu^{3+} is quite weak under this wavelength excitation (the red dashed curve). Meanwhile, the wavelength 394 nm corresponds to the $\text{Eu}^{3+} {}^7\text{F}_0 \rightarrow {}^5\text{L}_6$ transition, which is also close to the onset of the Eu^{2+} 4f–5d absorptions, so the emission intensities of both Eu^{2+} and Eu^{3+} ions are compatible (the blue dash-dot curve). In addition, the Eu^{3+} intensity under 276 nm excitation is stronger than that of Eu^{2+} , which implies that the contribution of the CTB of Eu^{3+} to the absorption at this wavelength is larger than that of the Eu^{2+} f-d transition (the black solid curve).

The vacuum referred binding energy (VRBE) scheme gives us a hint for the understanding of the valence stabilities of $\text{Eu}^{2+/3+}$ ions in $\text{CaMgSi}_2\text{O}_6$. Fig. S7† shows the updated VRBE scheme of lanthanide ions in $\text{CaMgSi}_2\text{O}_6$ constructed using the experimental data including the band exciton creation energy of $\text{CaMgSi}_2\text{O}_6$ (~ 157 nm, 7.90 eV), the $\text{Eu}^{3+}\text{--O}^{2-}$ charge transfer band (CTB) energy (~ 239 nm, 5.19 eV), the energies of five f-d excitation bands [~ 325 nm (3.81 eV), ~ 290 nm (4.27 eV), ~ 245 nm (5.06 eV), ~ 214 nm (5.79 eV) and ~ 193 nm (6.42 eV)] of Ce^{3+} , and the exchange splitting energy (0.91 eV) between the high spin [~ 228 nm (5.44 eV)] and low spin [~ 274 nm (4.53 eV)] 5d states of Tb^{3+} shown in Fig. S8.†^{22,36}

Hence, the Coulomb repulsion energy $U(\text{CaMgSi}_2\text{O}_6)$ due to the chemical environment of $\text{CaMgSi}_2\text{O}_6$, which corresponds to the difference between the ground state 4f-shell electron binding energy of Eu^{2+} and Eu^{3+} , is calculated as ~ 7.03 eV.³⁷

With the guidance of this VRBE scheme, the valence stabilities of the $\text{Eu}^{2+}/\text{Eu}^{3+}$ are envisaged to relate to the energy difference (E_{FF}) between the 4f ground state of Eu^{2+} ion and the Fermi energy level that is assumed to be located midway between the top of the valence band and the bottom of the conduction band of the host compound. The reducing synthetic conditions such as CO or H_2 ambiances would raise the Fermi level, resulting in a smaller E_{FF} value and more stable Eu^{2+} valence, while the oxidizing conditions in air plays the contrary role.³⁸ Empirically, when Eu replaces the alkaline-earth site in complex-oxide hosts and the E_{FF} value is smaller than ~ 1.50 eV, the doping Eu ions can be reduced to +2 valence under reducing, neutral, and even oxidizing atmospheres. The smaller the value of E_{FF} , the larger the $\text{Eu}^{2+}/\text{Eu}^{3+}$ ions ratio tends to be. For example, in the case of $\text{SrB}_4\text{O}_7:\text{Eu}$, the E_{FF} value is close to zero, the dominant Eu^{2+} valence can be obtained by heating in the neutral (N_2) ambience or in air. However in the case of $\text{CaO}:\text{Eu}$, the E_{FF} value of ~ 1.20 eV, Eu enters as Eu^{3+} together with a small concentration of Eu^{2+} . In the present case of $\text{CaMgSi}_2\text{O}_6:\text{Eu}$, the E_{FF} value is estimated to be 0.93 eV from the VRBE scheme in Fig. S7,[†] which falls between the two former cases. Consequently, it is envisaged that a considerable amount of Eu^{2+} ions could be stable when the samples are synthesized under a N_2 ambience, which paves a convenient way to achieve the co-existence of Eu^{2+} and Eu^{3+} luminescence.

3.5. The excitation-wavelength and the temperature driven colour evolution

We have observed that under an appropriate wavelength excitation, the main emission either from Eu^{2+} or from Eu^{3+} , or comparable emission intensities from both of Eu^{3+} and Eu^{2+} can be observed by the samples prepared in a N_2 inert ambience. Fig. 5b presents the CIE colour coordinates and lumines-

cent images of the $\text{Ca}_{0.98}\text{Eu}_{0.02}\text{MgSi}_2\text{O}_6$ sample prepared in a N_2 inert ambience under 276, 343, 394 nm excitation, showing the evident variations of the emitting-colour under different wavelength excitations. Because the emission of Eu^{2+} is in the blue range and that of Eu^{3+} in the red region, the excitation-wavelength driven colour evolution is realized.

Furthermore, the temperature driven colour evolution of the $\text{Ca}_{0.98}\text{Eu}_{0.02}\text{MgSi}_2\text{O}_6$ sample synthesized under a N_2 ambience is also investigated in consideration of the different thermal stabilities of Eu^{2+} and Eu^{3+} luminescence in $\text{CaMgSi}_2\text{O}_6$ as mentioned in sections 3.2 and 3.3. The excitation wavelength of 304 nm is selected because the corresponding emission curve contains both the emissions of Eu^{2+} and Eu^{3+} with similar peak intensities. Fig. 6a shows the emission ($\lambda_{\text{ex}} = 304$ nm) spectra in the temperature range of 330–505 K. With the increase of temperature, the red emission of Eu^{3+} ions with superior thermal stability turns prevailing while the blue emission of Eu^{2+} ions gradually decreases, which implies a temperature driven colour evolution of the sample from pink to red. The corresponding CIE colour coordinates are shown in Fig. 6b.

Considering the excitation-wavelength and the temperature driven colour evolution properties of the $\text{Ca}_{0.98}\text{Eu}_{0.02}\text{MgSi}_2\text{O}_6$ sample synthesized under a N_2 ambience, its possible application in anti-counterfeiting is demonstrated below. The $\text{Ca}_{0.98}\text{Eu}_{0.02}\text{MgSi}_2\text{O}_6$ sample was first distributed in a glass mold to form the vivid pattern as displayed in Fig. 7. The commonly used excitation wavelengths (254 and 365 nm) and temperature from 330 to 505 K were used as the two factors to control the colour of pattern.

At the column excited by 365 nm, with the increase of temperature, the colour of the pattern turns from blue to purple; while excited by 254 nm, the colour pattern seems quite stable as red with rising temperature; under the co-excitation of 254 and 365 nm, the pattern changes from purple to pink colour. These phenomena indicate that by applying the controlling factors of excitation wavelength and temperature, diverse colour evolutions could be achieved, which might be beneficial

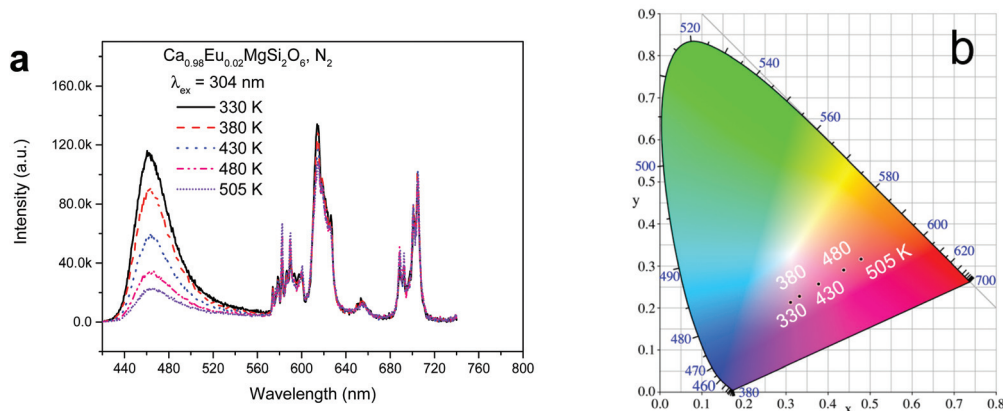


Fig. 6 (a) Emission ($\lambda_{\text{ex}} = 304$ nm) spectra of $\text{Ca}_{0.98}\text{Eu}_{0.02}\text{MgSi}_2\text{O}_6$ sample synthesized under N_2 ambience in the temperature range of 330–505 K and (b) corresponding CIE colour coordinates.



Fig. 7 Luminescent images of patterns formed by $\text{Ca}_{0.98}\text{Eu}_{0.02}\text{MgSi}_2\text{O}_6$ sample synthesized under N_2 ambience with different excitation wavelength and temperature.

for the multi-levels of anti-counterfeiting with the help of sophisticated pattern design.

Conclusions

In this work, the structure, luminescence and excitation-wavelength/temperature driven colour evolution properties of $\text{CaMgSi}_2\text{O}_6:\text{Eu}^{2+}$, $\text{CaMgSi}_2\text{O}_6:\text{Eu}^{3+}$ and $\text{CaMgSi}_2\text{O}_6:\text{Eu}^{2+/3+}$ samples were studied in detail. The Rietveld refinement shows that the synthesized $\text{CaMgSi}_2\text{O}_6$ host possesses a monoclinic purity phase with the $C2/c$ space group. The refined lattice parameters are $a = 9.747(1) \text{ \AA}$, $b = 8.932(1) \text{ \AA}$, $c = 5.249(1) \text{ \AA}$, and $\beta = 105.9^\circ$. The Eu^{2+} luminescence is found to have the lowest relaxed 5d energy level at $\sim 409 \text{ nm}$, a single narrow emission band at $\sim 451 \text{ nm}$ with a FWHM value of 0.20 eV and a Stokes shift value of $\sim 0.28 \text{ eV}$. The Eu^{2+} blue emission also has a relatively poor thermal stability with an average thermal activation energy of $\sim 0.30 \text{ eV}$, which is approximate to the energy gap ($\sim 0.39 \text{ eV}$) between the lowest 5d excitation level of Eu^{2+} and the bottom of conduction band in the VRBE scheme. As for the Eu^{3+} luminescence, it shows red emission with a good thermal stability under a $\text{Eu}^{3+}-\text{O}^{2-}$ charge-transfer excitation at $\sim 239 \text{ nm}$. Finally, considering that the Eu^{2+} and Eu^{3+} emissions exhibit different excitation wavelengths, emission colour and thermal stability, the designed sample is synthesized in a N_2 ambience to achieve the co-existence of Eu^{2+} and Eu^{3+} luminescence with the guidance of the E_{FF} value ($\sim 0.93 \text{ eV}$) from the VRBE scheme. By tuning the excitation-wavelength and temperature, the designed sample shows the controllable colour evolution in several colours including red, pink, purple and blue. A vivid pattern is also depicted using this sample to demonstrate its potential application in anti-counterfeiting.

Author contributions

Conceptualization, H.L.; Data curation, F.S. and Z.Q.; Formal Analysis, F.S., C.D., M.B., P.D. and H.L.; Funding acquisition,

C.D., M.B. and H.L.; Investigation, F.S.; Methodology, F.S. and H.L.; Project administration, H.L.; Resources, H.L.; Supervision, H.L.; Validation, F.S. and H.L.; Visualization, F.S., Y.Y. and Y.O.; Writing – original draft, F.S. and W.Z.; Writing – review and editing, F.S., W.Z., Y.Y., Y.O., Z.Q., C.D., M.B., P.D. and H.L.

Conflicts of interest

There are no conflicts to declare.

Acknowledgements

This work was financially supported by the National Natural Science Foundation of China (Grant No. 21671201, U1632101, 61635012 and 11974338). The measurements on the vacuum ultraviolet (VUV) spectra of the samples were carried out with the support of the 4B8 beamline at the Beijing Synchrotron Radiation Facility (BSRF). The numerical calculations in this paper were partially performed on the supercomputing system in the Supercomputing Centre of the University of Science and Technology of China. M.G.B. acknowledges the support from the Chongqing Recruitment Program for 100 Overseas Innovative Talents (Grant No. 2015013), the Program for the Foreign Experts (Grant No. W2017011) and Wenfeng High-end Talents Project (Grant No. W2016-01) offered by Chongqing University of Posts and Telecommunications (CQUPT), Estonian Research Council grant PUT PRG111, European Regional Development Fund (TK141) and NCN project 2018/31/B/ST4/00924.

Notes and references

- P. Kumar, S. Singh and B. K. Gupta, *Nanoscale*, 2016, **8**, 14297–14340.
- X. W. Liu, Z. G. Yi, X. Qin, H. Liu, W. Huang and X. G. Liu, *Adv. Opt. Mater.*, 2019, **7**, 1900519.
- Z. Zhuo, Y. S. Liu, D. J. Liu, P. Huang, F. L. Jiang, X. Y. Chen and M. C. Hong, *Chem. Sci.*, 2017, **8**, 5050–5056.
- P. X. Pei, P. B. Duanmu, B. B. Wang, X. Miao, C. Zhang and W. S. Liu, *Dalton Trans.*, 2021, **50**, 3193–3200.
- P. P. Du, S. Y. Li, X. J. Wang, Q. Zhu and J.-G. Li, *Dalton Trans.*, 2021, **50**, 3337–3347.
- R. F. Zhou, F. K. Ma, F. Su, Y. Y. Ou, Z. M. Qi, J. H. Zhang, Y. Huang, P. Dorenbos and H. B. Liang, *Inorg. Chem.*, 2020, **59**, 17421–17429.
- H. J. Guo, T. Seto, T. Geng, B. Zou, G. S. Li, Y. Uwatoko, Z. B. Tang, Z. B. Li and Y. H. Wang, *Dalton Trans.*, 2020, **49**, 8056–8059.
- P. Dorenbos, *J. Phys.: Condens. Matter*, 2003, **15**, 575–594.
- R. J. Xie, N. Hirosaki and M. Mitomo, *Appl. Phys. Lett.*, 2006, **89**, 241103.
- X. J. Zhang, Y.-T. Tsai, S.-M. Wu, Y.-C. Lin, J.-F. Lee, H.-S. Sheu, B.-M. Cheng and R.-S. Liu, *ACS Appl. Mater. Interfaces*, 2016, **8**, 19612–19617.

- 11 M. M. Shang, S. S. Liang, N. R. Qu, H. Z. Lian and J. Lin, *Chem. Mater.*, 2017, **29**, 1813–1829.
- 12 J. W. Qiao, L. X. Ning, M. S. Molokeev, Y.-C. Chuang, Q. Y. Zhang, K. R. Poeppelmeier and Z. G. Xia, *Angew. Chem., Int. Ed.*, 2019, **58**, 11521–11526.
- 13 Z. C. An, S. T. Che, Y. H. Song, X. T. Zhang, R. J. Dong, D. Zhang, X. Q. Zhou, Z. Shi and H. F. Zou, *Inorg. Chem.*, 2020, **59**, 790–4799.
- 14 S. H. Lee, J. H. Park, S. M. Son and J. S. Kim, *Appl. Phys. Lett.*, 2006, **89**, 221916.
- 15 Y.-I. Kim, W. B. Im and D. Y. Jeon, *J. Mater. Sci.*, 2006, **41**, 1643–1647.
- 16 T. Kida, M. M. Rahman and M. Nagano, *J. Am. Ceram. Soc.*, 2006, **89**, 1492–1498.
- 17 P. Chandrakar, D. P. Bisen, R. N. Baghel and B. P. Chandra, *J. Electron. Mater.*, 2015, **44**, 3450–3457.
- 18 M. A. Matos, H. F. Brito, L. C. V. Rodrigues, V. R. Morais and C. Yamagata, *Mater. Sci. Forum*, 2016, **88**, 30–34.
- 19 A. A. Coelho, *Topas Academic, version 4, Coelho Software*: Brisbane, Australia, 2005.
- 20 Y.-I. Kim, S.-H. Nahm, W. B. Im, D. Y. Jeon and D. H. Gregory, *J. Lumin.*, 2005, **115**, 1–6.
- 21 R. D. Shannon, *Acta Crystallogr., Sect. A: Cryst. Phys., Diffraction, Theor. Gen. Crystallogr.*, 1976, **32**, 751.
- 22 F. Su, B. B. Lou, Y. Y. Ou, Y. L. Yang, W. J. Zhou, C.-K. Duan and H. B. Liang, *J. Phys. Chem. C*, 2021, **125**, 5957–5967.
- 23 P. Dorenbos, *J. Phys.: Condens. Matter*, 2003, **15**, 4797.
- 24 A. Meijerink and G. Blasse, *J. Lumin.*, 1989, **43**, 283–289.
- 25 C. K. Duan and M. F. Reid, *J. Solid State Chem.*, 2003, **171**, 299–303.
- 26 Y. H. Wang, M. G. Brik, P. Dorenbos, Y. Huang, Y. Tao and H. B. Liang, *J. Phys. Chem. C*, 2014, **118**, 7002–7009.
- 27 G. Blasse and B. Grabmaier, *Luminescent Materials*, Springer Verlag: Berlin, 1994.
- 28 M. Nazarov, B. Tsukerblat and D. Y. Noh, *J. Phys. Chem. Solids*, 2008, **69**, 2605–2612.
- 29 B. Henderson and G. F. Imbusch, *Optical Spectroscopy of Inorganic Solids*, Clarendon Press, Oxford, U.K., 1989.
- 30 P. Dorenbos, *Opt. Mater.*, 2017, **69**, 8–22.
- 31 H. H. Lin, H. B. Liang, Z. F. Tian, B. Han, J. Wang, Q. Su and G. B. Zhang, *J. Phys. D: Appl. Phys.*, 2009, **42**, 165409.
- 32 E. Glais, F. Massuyeau and R. Gautier, *Chem. – Eur. J.*, 2021, **27**, 905–914.
- 33 Z. C. An, W. Liu, Y. H. Song, X. T. Zhang, R. J. Dong, X. Q. Zhou, K. Y. Zheng, Y. Sheng, Z. Shi and H. F. Zou, *J. Mater. Chem. C*, 2019, **7**, 6978.
- 34 Y. D. Ma, X. S. Peng, M. Z. Fei, W. N. Zhang, L. M. Teng, F. F. Hu, R. F. Wei and H. Guo, *J. Alloys Compd.*, 2020, **846**, 156435.
- 35 T. Zheng, M. Runowski, P. Woźny and S. Lis, *J. Alloys Compd.*, 2020, **822**, 153511.
- 36 P. Dorenbos, *J. Lumin.*, 2020, **222**, 117164.
- 37 P. Dorenbos, *J. Lumin.*, 2013, **135**, 93–104.
- 38 P. Dorenbos, *J. Phys.: Condens. Matter*, 2005, **17**, 8103–8111.